Capano G, Penfold TJ, Chergui M, Tavernelli I.

Photophysics of a Copper Phenanthroline Elucidated by Trajectory and Wavepacket-based Quantum Dynamics: A Synergetic Approach.

***Physical Chemistry Chemical Physics* 2017**

DOI:

PCCP

Accepted Manuscript

This article can be cited before page numbers have been issued, to do this please use: G. Capano, T. J. Penfold, I. Tavernelli and M. Chergui, *Phys. Chem. Chem. Phys.*, 2017, DOI: 10.1039/C7CP00436B.

ROYAL SOCIETY OF CHEMISTRY

rsc.li/pccp

View Article Online
DOI: 10.1039/C7CP00436B
ROYAL SOCIETY OF CHEMISTRY

Journal Name

ARTICLE TYPE

Cite this: DOI: 10.1039/xxxxxxxxxx

Photophysics of a Copper Phenanthroline Elucidated by Trajectory and Wavepacket-based Quantum Dynamics: A Synergetic Approach

G. Capano[a], T.J. Penfold,*[b], M. Chergui[a] and I. Tavernelli*[c]

Received Date
Accepted Date

DOI: 10.1039/xxxxxxxxxx

www.rsc.org/journalname

On-the-fly excited state molecular dynamics is an attractive method for studying non-equilibrium processes in excited states and is beginning to emerge as a mature approach much like its ground state counterparts. In contrast to quantum wavepacket dynamics methods, it negates the need for modelling potential energy surfaces, which usually confine nuclear motion within a reduced number of vibrational modes. In addition, on-the-fly molecular dynamics techniques are easily combined with the atomistic description of the solvents (through the QM/MM approach) allowing to explicitly address the effect of the environment. Herein, we study the nonadiabatic relaxation of photoexcited $[Cu(dmp)_2]^+$ (dmp = 2,9-dimethyl-1,10-phenanthroline) using QM/MM Trajectory Surface Hopping (TSH). We show that the decay of the initially excited singlet state into the lowest singlet (S_1) state occurs within 100 fs, in agreement with previous experiments, and is slightly influenced by the nature of the solvent. Using principal component analysis (PCA), we also identify the dominant normal modes activated during the excited state decay, which are then used to design the vibrational Hamiltonian for quantum wavepacket dynamics simulations.

1 Introduction

Owing to its rigorous treatment of quantum nuclear effects, quantum dynamics on electronically excited state potential energy surfaces (PES) has traditionally been computed using quantum nuclear wavepacket approaches[1,2]. Indeed, these simulations have contributed significantly to our understanding of fundamental photophysical and photochemical processes[3–9]. However, despite the development of sophisticated algorithms, such as the multi-configurational time-dependent Hartree (MCTDH) approach[10], the exponential scaling of the computational effort with the number of degrees of freedom combined with the requirement to pre-compute the coupled potentials energy surfaces have generally restricted these simulations to model Hamiltonians, which only include the nuclear degrees of freedom deemed most appropriate for the dynamics. The choice of the coordinates, which span a subspace of full nuclear coordinate space, is therefore one of the most critical steps that determine the accuracy of this type of simulations. This subspace can be deduced based on symmetry and physical considerations[11,12] but the selection of the most relevant set of modes can still, to a greater or lesser extent, rely on empirical *trial and error* approaches . Therefore, a guarantee on the quality of the selected coordinates for the description of the dynamics of interest is often lacking, placing great emphasis upon studying the limitations of each particular model potential. In addition, quantum dynamics methods usually treat solvents at the level of a harmonic bath modelled by an ensemble of harmonic oscillators[13,14], as an explicit description is still computationally unaffordable. While this approach can be adequate in many situation for which the solvent does not play a direct role, in other cases the relevance of the solute-solvent interaction is such that a more accurate atomistic representation of the solvent is required[15].

Ab initio molecular dynamics (AIMD), which emerged following the pioneering work of Car and Parrinello[16], has become a firmly established technique for the simulation of ground state properties of molecules, liquids and solids. Importantly, as the nuclei are treated classically, in AIMD the system evolves according to Newton's equations of motion and therefore the propagation only requires, at each step, the energy and the gradient of the PES in a single point in nuclear configuration space. The success of this approach naturally led to its extension to the description of the out-of-equilibrium dynamics of photoexcited systems. In this case, the most pertinent difference from ground state AIMD is the requirement to include nonadiabatic effects arising from the breakdown of the Born-Oppenheimer approximation[2]. While

[a] *Laboratory of Ultrafast Spectroscopy and Lausanne Centre for Ultrafast Science (LACUS), ISIC, École polytechnique Fédérale de Lausanne (EPFL), 1014 Lausanne, Switzerland*
[b] *School of Chemistry, Newcastle University, Newcastle upon Tyne, NE1 7RU, United Kingdom. tom.penfold@ncl.ac.uk*
[c] *IBM Research Laboratory Zürich, Rüschlikon, Switzerland. ivano3467@gmail.com*

View Article Online
DOI: 10.1039/C7CP00436B

various approaches have been developed to address such transitions[17], Tully's Trajectory Surface Hopping (TSH)[18,19] approach has become the most popular one due to its favourable balance between efficiency and accuracy. In TSH, the nuclear wavepacket is replaced with a swarm of classical trajectories. Nonadiabatic coupling effects are included by means of trajectory *hops* between different PES, which are governed by a surface hopping algorithm designed by Tully[18]. The condition of spatial locality enforced by the discretization of the wavepacket makes it easy to calculate electronic properties of the system *on-the-fly* at each time step. This means that simulations which allow the system to evolve into the fully unconstrained configurational space of the system are possible. Moreover, this method can easily be combined with a QM/MM scheme[15], which treats explicitly the solute/solvent interactions[20].

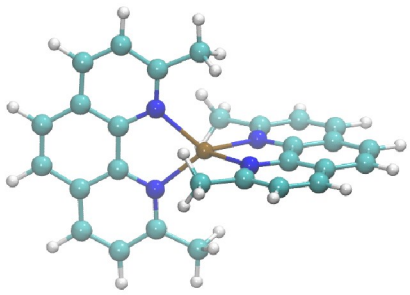

Fig. 1 Schematic of $[Cu(dmp)_2]^+$. In the ground state the two phenanthroline ligands are perpendicular. Color code: Cu atom (brown), N atoms (blue), C atoms (cyan), and H atoms (white).

Despite the mentioned advantages of full configuration space simulations (such as *on-the-fly* TSH) they still require a large computational effort to research statistical convergence. In particular, in TSH a large number of trajectories is usually required (in the order of 10^3) and therefore the rigorous applicability of this approach remains limited to relatively small molecular systems (with no more than a couple of hundreds of atoms). Furthermore, quantum effects such as quantum decoherence cannot be captured due to the classical description of the nuclear dynamics and to the fact that trajectories are not allowed to interact with each other. This classical evolution also means that these simulations can offer no guarantee that increasing the number of trajectories will result in convergence on the correct solution.

Herein, we use a linear response time-dependent density functional theory (LR-TDDFT) based TSH scheme to study the photoexcited decay dynamics of a prototypical Cu(I) transition metal complexes $[Cu(dmp)_2]^+$(dmp = 2,9-dimethyl-1,10-phenanthroline) in solution (see Fig. 1). The same compound was already the subject of previous studies using a variety of experimental[21–26] and theoretical techniques[27–31]. In this work, we extend the analysis of the ultrafast photophysics of $[Cu(dmp)_2]^+$in solution using TSH dynamics. We show how in the full (unconstrained) configuration space the decay from the initially excited bright metal-ligand charge transfer (MLCT) state to the lowest S_1 state can occurs in the expected time scale (of $\sim$100 fs) through a series of surface hops among singlet and triplet potential energy surfaces. In addition, using the QM/MM framework we describe the role of the solvent in the ultrafast relaxation process. Finally, we perform a comparative study of the results obtained using TSH and the MCTDH approaches[27,28], emphasizing the importance of an accurate selection of the most relevant collective vibrational modes for the wavepacket propagation. In particular, using a principal component analysis (PCA) of the TSH trajectories, we are able to determine the main vibrational modes in $[Cu(dmp)_2]^+$activated during the first few hundreds of femtoseconds of dynamics following the photoexcitation, which are then used in the MCTDH dynamics. A comparison with the modes obtained from the normal mode analysis at the ground state optimized structures[27,28] confirms the validity of this approach, which opens new avenues for the optimization and automatization of wavepacket propagation schemes.

2 Computational Methods

2.1 Excited State Molecular Dynamics

Nonadiabatic dynamics was performed using the LR-TDDFT-based TSH scheme[32–34] as implement in the CPMD code[35]. Electronic states were computed using the PBE exchange and correlation functional[36] and the Kohn-Sham orbitals were described by a plane wave basis set with a cut-off of 85 Ry. Martin-Trouiller pseudopotentials[37] with DCACP corrections to account for the dispersion interactions[38,39] were used to describe core-electrons. For each TSH trajectory, the initial frame was chosen randomly from a ground state Born-Oppenheimer (BO) Molecular Dynamics ensemble equilibrated at room temperature (300K) using the Nose-Hoover thermostat[40,41]. The electronic excited state used to start the TSH dynamics was selected as the one with the largest oscillator strengths among all excited states in the energy range between 1.5 and 2.6 eV. This energy range was selected according to experimental absorption studies[24,42], which identify the optical bright ^{1}MLCT state at around 2.6 eV. The nonadiabatic dynamics were carried out with a time step of 5 a.u. ($\sim$0.12 fs). Nine trajectories were run using the classical TSH algorithm, according to which only transitions between states of the same spin multiplicity (internal conversion) can be described. In our case, since the trajectories were initiated in a photoexcited singlet state, only nonadiabatic transitions between singlet excited states were possible. In order to evaluate ISC probabilities, spin-orbit coupling (SOC) elements, and Landau-Zener probabilities were calculated at the crossing points between the actual force state (singlet) and all energetically close triplet states (the force state is defined as the electronic state in TSH from which the nuclear forces are computed). To monitor the SOC time evolution, in two cases SOC were also evaluated along the entire trajectory with a frequency of 1 fs^{-1}. For comparative purposes, one extra trajectory was propagated using the recently implemented TSH/ISC scheme[43], which allows for the *on-the-fly* calculation of the SOCs and corresponding Landau-Zener transition probabilities between states of different spin multiplicities. All molecular dynamics simulations (BO and TSH) were performed within the QM/MM scheme[44] where the $[Cu(dmp)_2]^+$ complex was described at DFT/TDDFT level while the solvent (acetonitrile) was treated classically with

View Article Online
DOI: 10.1039/C7CP00436B

the Amber force field[45]. The electrostatic and van der Waals interactions between the quantum and the classical subsystems were explicitly included as described in Ref.[46].

2.2 Principal Components Analysis of TSH Trajectories

One of the advantages of TSH dynamics is that it can sample the entire (unconstrained) configuration space of the system, without the need of imposing a subset of collective variables as it is usually the case for quantum wavepacket dynamics. However, to reach statistical convergence with TSH dynamics a large number of trajectories is required (in the order of 10^3), making the method unsuited for the simulation of molecular systems with more than a few hundred of atoms. These limitations make it very appealing to combine mixed quantum classical trajectory-based approaches (such as TSH dynamics) with the more accurate, but spatially confined, quantum wavepacket dynamics (such as MCTDH).

Consequently, herein we propose to use TSH dynamics for the automatic determination of the most important nuclear degrees of freedom, which can then be developed into a model Hamiltonian for wavepacket dynamics, such as MCTDH. Our approach is based on the principal component analysis (PCA)[47–49] of the TSH trajectories, which provides a set of collective modes ordered according to their relevance (weights) that can then be projected onto the basis of molecular normal modes (vibrational modes) evaluated, for instance, at the ground state optimized geometry.

In molecular dynamics, PCA is based upon the diagonalization of the covariant matrix of the nuclear displacements

$$C_{ij} = \langle (R_i(t) - \langle R_i \rangle)(R_j(t) - \langle R_j \rangle) \rangle \tag{1}$$

where $R_i(t)$ is the i-th coordinate of the collective position vector $\mathbf{R}(t)$ in the molecular configuration space of dimension $3N_a$ ($\mathbf{R}(t) \in \mathbb{R}^{3N_a}$, where N_a is the number of atoms). The parentheses $\langle\rangle$ represent the ensemble average, which in the case of MD simulations is approximated by the time average. The covariance matrix $\mathbf{C}$ with elements C_{ij} is a square matrix of dimension $3N_a \times 3N_a$ and is symmetric with respect to the main diagonal, meaning that it has real eigenvalues and the eigenvectors are orthogonal to each other. The diagonalization of the covariant matrix

$$\mathbf{C}\mathbf{v}_i = \lambda_i \mathbf{v}_i \,, \tag{2}$$

leads a set of eigenvalues λ_i and eigenvectors $\mathbf{v}_i \in \mathbb{R}^{3N_a}$, ($i = 1, \ldots, 3N_a$). Each eigenvalue corresponds to the mean square fluctuation along the corresponding eigenvector or principal component, and describes its contribution to the total fluctuation. The eigenvectors are ordered such that their eigenvalues are in decreasing order, with the first one (the first principal component) corresponding to the largest displacement. By normalizing the sum of all eigenvalues to 1, we can define the number of eigenvalues i_m required to describe 90% of the total dynamics: $\sum_{i=1}^{i_m} \lambda_i = 0.9$. In most cases, the first 10 PCs are often enough to reach this threshold.

The most relevant m eigenvectors $\mathbf{v}_i$ ($i = 1, \ldots, i_m$) can be used to select the vibrational modes that are relevant for the description of the dynamics in the excited state. Using the projection between the principal component $\mathbf{v}_i$ and the normal mode $\mathbf{d}_k \in \mathbb{R}^{3N_a}$

$$p_{i,k} = (\mathbf{v}_i \cdot \mathbf{d}_k) \tag{3}$$

the relevant normal modes are the ones which have the largest overlap with the relevant PCs (we use the standard scalar product in the $3N_a$ dimensional Euclidean space). To visualise the different principal components, it is possible to associate to each PC a meta-trajectory obtained through the projection of the original trajectory $\mathbf{R}(t)$

$$\mathbf{R}_{[i]}(t) = (\mathbf{v}_i \cdot \mathbf{R}(t)) \,. \tag{4}$$

3 Results

3.1 Femtosecond Nonadiabatic Decay of $[Cu(dmp)_2]^+$

A summary of the main characteristics of all nine TSH trajectories simulating the photoexcited decay of $[Cu(dmp)_2]^+$ following excitation into the lowest optically bright ^{1}MLCT state is shown in Table 1. The number of crossing points between singlet and triplet states (number of possible ISC events) and the corresponding cumulative ISC probabilities are also shown. For each trajectory, the initial singlet state (force state at t=0 fs) is reported together with the corresponding excitation energy. The final state (force state after 100 fs) was found to be S_1 in all simulations, i.e. the lowest singlet MLCT state. The initial singlet state was chosen to be the singlet state with the largest oscillator strength at the specific starting geometry. While the numbering of this state varies (see Table 1) for the different starting configurations (due to the high density of bright and dark states) this does not affect the decay rate, as shown by the fact that all trajectories end up in the S_1 state within 100 fs of dynamics. It is also noted that due to the presence of spin-orbit coupling (SOC), direct excitation into the triplet manifold is possible. However, for this type of Cu complexes the SOCs are not sufficiently large for this to play a significant role during excitation and consequently the direct excitation into triplet states has been neglected in our simulations.

Fig. 2 shows the force (singlet) states plotted together with the other singlet and triplet state energy profiles for three representative trajectories simulated using the TSH algorithm as implemented in the CPMD[35] code. The initial states are S_6, S_4, and S_6, respectively. The remaining six trajectories show similar profiles and the key information is summarized in Table 1. This fast relaxation process that follows the photoexcitation is made possible by the occurrence of a large number of surface hops within the singlet states manifold. The TSH algorithm used for these simulations allows for nonadiabatic transitions between states with equal spin-multiplicity (singlet states in this case) while spin-flip transitions (i.e. intersystem crossings) are not explicitly included.

The latter requires a generalization of the nonadiabatic transition probabilities that includes the calculation of the SOCs and intersystem crossing (ISC) probabilities. Even though this type of dynamics has recently been successfully implemented[43,50–54] it is not yet applicable (in the fully converged manner) to metal complexes of the size of the $[Cu(dmp)_2]^+$ complex in solution. Consequently, in this work the ISC probabilities have been estimated, *a posteriori*, at the crossing points between singlet and

View Article Online
DOI: 10.1039/C7CP00436B

Table 1 Characterization of the initial (0 fs) force state (singlet) with corresponding energy for the 9 TSH trajectories. The count of the occurring ISC events, and corresponding cumulative ISC probability (during 100 fs of dynamics) for all trajectories is also shown. The ISC probabilities are computed *a posteriori* using the Landau-Zener formula in Eq. 5.

Trajectory	Initial state		No. Crossing	Probability
	index	E (eV)	points	of ISC
1	S_6	2.050	10	28.4 %
2	S_4	1.977	14	54.7 %
3	S_6	2.040	11	99.9 %
4	S_6	2.009	14	36.0 %
5	S_7	2.097	6	4.3 %
6	S_7	2.119	20	98.6 %
7	S_7	2.150	15	12.2 %
8	S_4	1.868	9	97.6 %
9	S_7	2.194	11	46.4 %

triplet states using the Landau-Zener approach. It is stressed that this is an estimate and therefore caution should be applied in not over-interpreting these ISC probabilities.

In the Landau-Zener approach, the transition probability between a singlet state S_i and a triplet state T_k is given by

$$p_{ik} = 1 - e^{-2\pi\Gamma_{ik}} \tag{5}$$

where

$$\Gamma_{ik} = \frac{|\langle\Psi_i|H^{SO}|\Psi_k\rangle|^2}{\Delta E_{S-T}/dt} \tag{6}$$

and ΔE_{S-T} is the absolute value of the energy gap between the two states evaluated in the spin-diabatic representation[43]. The total probability for an ISC to occur along a full trajectory is computed as

$$P = p_1 + \sum_{i=2}^{N} p_i \prod_{j=1}^{i-1}(1-p_j), \tag{7}$$

where the indices i and j run over the number N of crossings between the force state (red line in Fig. 2) and the manifold of energetically close-lying triplet states. For the three trajectories shown in Fig. 2, P amounts to 28.42 %, 54.73 % and 99.93 %, respectively. The complete set of cumulative ISC probabilities is reported in Table 1. The upper panels of Fig. 2 show the Landau-Zener probability for the three selected trajectories (green lines) together with the cumulative ISC probabilities as a function of time (black lines). From this analysis, we observed that the average cumulative probability is about 53 %, meaning that more than half of the trajectories would undergo at least one ISC event during the first 100 fs of dynamics; this is in agreement with recent conclusions based on quantum wavepacket dynamics[30].

Finally, in Fig. 3 we report the time evolution of a single trajectory carried out using the extended (and computationally more expensive) TSH/ISC scheme[43], which computes *on-the-fly* singlet and triplet excited state energies, SOC between the force state and the energetically closest states with different spin multiplicity, nonadiabatic Tully's probabilities (for IC events), and Landau-Zener probabilities (for ISC events).

Starting from the photoexcited S_6 state, the system relaxes

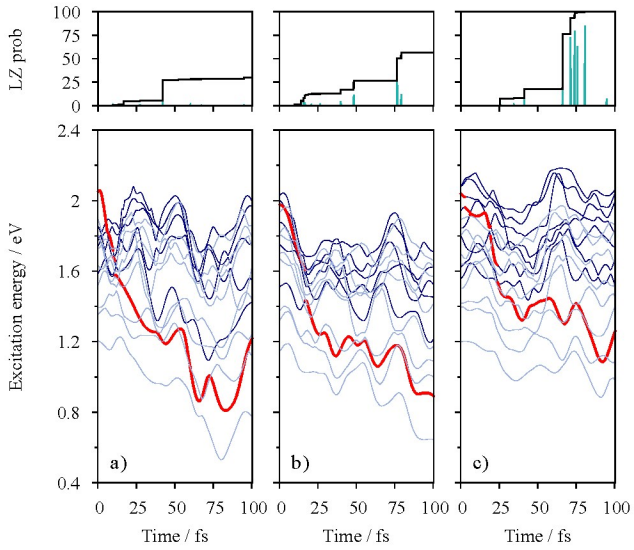

Fig. 2 Three typical TSH trajectories of the photoexcited decay of $[Cu(dmp)_2]^+$ following excitation into the optically bright ^{1}MLCT state. The dynamics are within the manifold of singlet states, while triplet states are computed from snap-shots sampled with a time interval of ~1 fs. Color code: singlet states (blue), triplet states (light blue), force state (red). *Top*) Landau-Zener probability (cyan) and cumulative probability (black) of ISC.

within 100 fs into the lowest excited state (S_1) through a series of surface hops that involve both singlet and triplet states. Notably, at around 13 fs of dynamics the trajectory first hops into the S_4 state followed after 10 fs, by a ISC into T_8 (top right zoom in Fig. 3) and a subsequent IC into the lower-lying triplet state T_7. Another ISC event occurs at 40 fs, which brings back the system into the manifold of singlet states where the relaxation proceeds, through several further surface hops, until S_1 is reached. At around 65 fs, the force state (S_1) approaches T_2, however without crossing it (bottom right zoom in Fig. 3). Interestingly, in the last 30 fs of dynamics the force state (S_1) and closest triplet state (T_1) proceed almost in parallel. This is in agreement with static calculations, which show that the lowest singlet and triplet states in the $[Cu(dmp)_2]^+$ complex, at the optimized triplet geometry, have the same MLCT character[22] and similar PESs topologies. Despite this fact, molecular distortions induced by thermal relaxation and by the interaction with the solvent can potentially trigger favourable ISC events between S_1 and T_1 on a longer time scale.

3.2 Solvent Effects on the Photoexcited Dynamics of $[Cu(dmp)_2]^+$

One of the principal goals of this study is to investigate how the explicit inclusion of the solvent, within the QM/MM coupling scheme, affects the excited state dynamics and can help to rationalize experimental observations, such as the extremely low quantum yield that characterizes this class of complexes in solution.

The simulations described so far deal with the TSH dynamics of $[Cu(dmp)_2]^+$ in acetonitrile. In this section, we compare one

View Article Online
DOI: 10.1039/C7CP00436B

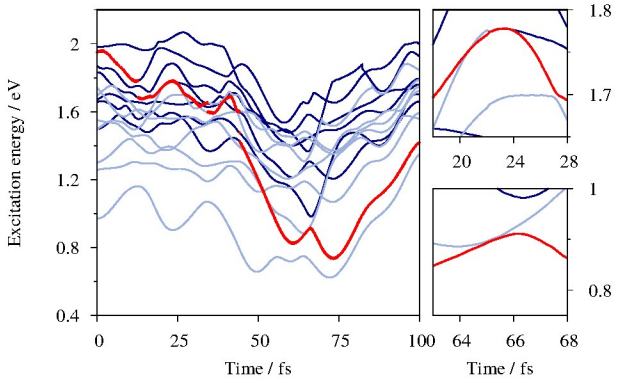

Fig. 3 (*Left*) Photoexcited decay of $[Cu(dmp)_2]^+$obtained from TSH/ISC dynamics. Color code: singlet states (blue), triplet states (cyan), force state (red). (*Right*) Zoom into two different time windows showing: a ISC event (top), and an avoided crossing (bottom).

of these trajectories with a new simulation initiated using exactly the same starting conditions (coordinates, velocities and excited state character) but performed in gas phase. Even though the dynamics is piecewise deterministic, the stochasticity of the surface hopping algorithm introduces randomness in the time evolution making therefore a direct comparison of the two trajectories (gas phase and liquid phase) not straightforward. However, a series of independent runs performed starting from different initial conditions confirms the overall trends obtained from this single trajectory analysis.

Fig. 4 (panels a and b) shows the comparison of the excited state energy profiles obtained for the gas and liquid phase simulations. In agreement with previous experiments[24], our results show a decay into the final S_1 state, which is largely independent of the environment. Unsurprisingly, the excited state energies in acetonitrile are lower than in the gas phase due to electrostatic induced stabilisation of the MLCT states. This reduces the energy gap to the ground state and will therefore, according to the energy gap law[55], increase the rate of the non-radiative decay. This observation further confirms the fact that, even at these ultrafast time scales (<100 fs), the solvent can induce important stabilisation effects (charge solvation) mediated by ultrafast relaxation (libration).

Collisions between the solute and the solvent molecules also provide important additional channels for the dissipation of the excess potential and kinetic energy stored in the photoexcited system upon photoexcitation. A closer inspection of Fig. 4 (right panel) reveals that the two structures that (by construction) were coinciding at $t = 0$ fs become noticeably different after 100 fs of dynamics. In particular, the ligand that acquires the extra electron in the MLCT transition undergoes a different distortion in solution than in the gas phase. This is mainly due to collisions with the nearby solvent molecules.

The overall distortion at the metal center can be monitored following the time evolution of the improper dihedral formed by the 4 nitrogen atoms coordinated to the Cu ion (Fig. 4, bottom right). In the gas phase, after a fast decay starting at the ground state average value of about 90° the dihedral angle oscillates (in a harmonic fashion) around an average value of about 75°. Differently, in solution due to the steric hindrance induced by the intercalating ligand the angular distortion is larger and in the longer time scale will lead to a further 'flattening' of the complex[24].

3.3 Principal Component Analysis of the Excited State Dynamics

As outlined in the introduction, the main advantage of trajectory based approaches over quantum wavepacket methods is that they can be relatively easily implemented in an *on-the-fly* scheme for the calculation of the ground and excited states energies and forces, which makes it possible to carry out simulations in the full, unconstrained, nuclear configuration space. However, the price to pay for this approach is associated with the difficulty of achieving statistical convergence in the number of trajectories. On the other hand, quantum wavepacket dynamics approaches (e.g. using MCTDH) are usually confined in a subspace (defined by a set of vibrational modes), which by nature is hard to define *a priori*. An interesting middle ground solution would consist of the possibility of using excited state molecular dynamics to select the most relevant normal modes activated during the dynamics, which can then be used to design a model Hamiltonian for the quantum wavepacket propagation.

In this section, we use the PCA applied to TSH trajectories to retrieve all of the relevant information about the vibrational normal modes activated during a particular photoexcited process. For the construction of the covariant matrix (Eq. 1) we used a subset of the atoms centred around the metal ion. In fact, a PCA performed on the entire set of atoms in $[Cu(dmp)_2]^+$will inevitably assign large intensities (weights) to all low frequency modes involving the bulky ligands. This because, the corresponding atomic displacements are such that their contribution dominates the construction of the covariance matrix. On the other hand, the investigated ultrafast dynamics will mainly deal with modes associated with the Cu-N bond stretches and distortions of the ligands geometry at the metal center. Consequently, for the present study, we restricted the PCA to the first eight neighbouring atoms of the Cu: four nitrogen and four carbon atoms. This relatively small set of atoms is capable of capturing all of the relevant molecular modes activated during the first ultrafast dynamics following photoexcitation, neglecting the effects of the modes associated to the thermal oscillations of the bulky ligands.

For each of the 9 TSH trajectory, the first two principal component (PC) eigenvectors of Eq. 2 were projected onto the normal modes computed at the optimised ground state structure of $[Cu(dmp)_2]^+$using Eq. 3. The projections, $p_{i,k}$ with $i = 1,2$ and $k = 1,\ldots,N_a$, were then multiplied by the corresponding PC eigenvalues giving the relative weights $\tilde{p}_{i,k} = p_{i,k}/\lambda_i$. Fig. 5a-c shows the relative weights ($\tilde{p}_{i,k}$) corresponding to the first 60 normal modes ($k = 1,\ldots,60$) computed for the three representative TSH trajectories (labelled *a*, *b* and *c*) used in the previous analysis (Fig. 2). The different colours correspond to different mode symmetries, A and B_3, while the vertical dotted lines are drawn in correspondence of the eight modes (labelled $\nu_8, \nu_{19}, \nu_{21}, \nu_{25}, \nu_{31}, \nu_{31}, \nu_{41}, \nu_{55}$, and ν_{58}) used in the MCTDH dy-

View Article Online
DOI: 10.1039/C7CP00436B

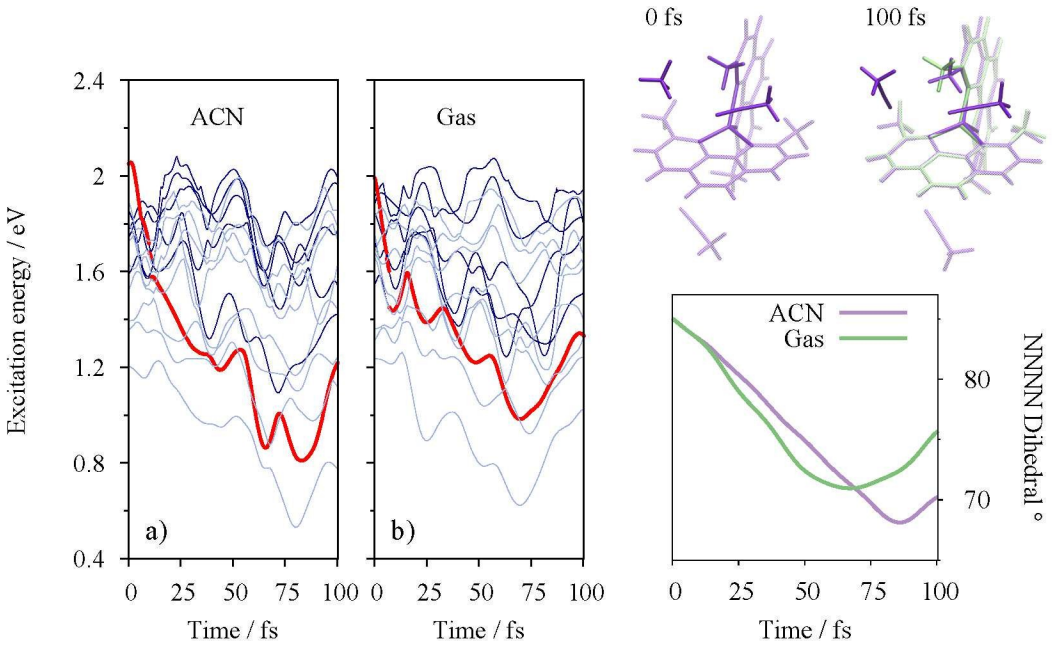

Fig. 4 (*Left*) Comparison between TSH trajectories of $[Cu(dmp)_2]^+$ computed in acetonitrile (ACN) (panel a)) and in gas phase (panel b). (*Righ-Top*) *Initial and final structures of* $[Cu(dmp)_2]^+$ *in solution (violet) and in gas phase (green). (Right-Bottom) Time series of the NNNN dihedral angle.*

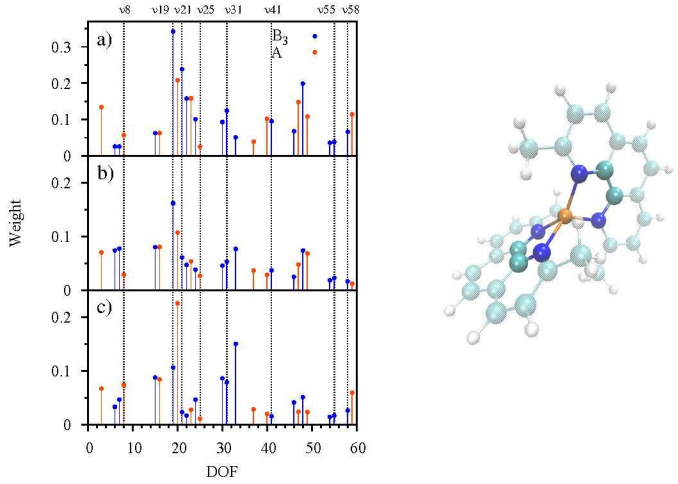

Fig. 5 (*Left*) Projection of the first 2 eigenvalues of the PCA onto the first 60 normal modes of $[Cu(dmp)_2]^+$ (symmetries: blue, B_3; red, A). (*Right*) Representation of $[Cu(dmp)_2]^+$ (transparent) and of the selected region (opaque) used to perform the PCA.

namics reported in refs.[27,28]. We observe that the set of important modes selected with PCA matches the one used in the quantum dynamics simulations[27], confirming the quality of our *a priori* choice of the relevant configuration *sub*space that defines the vibrational Hamiltonian. Nonetheless, there are additional modes that emerge from our analysis that were not included in the MCTDH dynamics. However, while potentially important, the effect of these modes on the dynamics of the $[Cu(dmp)_2]^+$ has still to be investigated. Notably, the total symmetric ν_{20} mode has a large weight in all trajectories considered, and in some cases it becomes even the dominant one. This mode corresponds to a symmetric bending of the angle defined by the nitrogen atoms of each ligand and the central copper.

To test the importance of this additional mode, we extended our previously reported model Hamiltonian[27,28] to include this additional mode, ν_{20}. The potential energy surfaces (ground and excited states) corresponding to the mode ν_{20} were computed using the B3LYP functional as described in[27,28] and are shown in the right hand panel of Fig. 6. These curves are fitted with a Morse potential defined as

$$V(Q) = D_0[\exp(k(Q-Q_0)-1)]^2, \qquad (8)$$

where the parameters D_0, k and Q_0 for each surface are reported in Table 2.

Table 2 Morse potential parameters for the additional normal mode ν_{20}.

	D_0 (eV)	$k \cdot 10^{-4}$ (a.u.)	Q_0 (a.u.)
S_1	99.051	60.793	-0.678
S_2	99.978	57.675	-0.701
S_3	98.094	60.162	-0.845

After excitation of the wavepacket into S_3, the population decay has been simulated with MCTDH as described in[27,28] using 4 different model Hamiltonians: (**1**) a 8-mode model Hamiltonian as reported in ref.[27], (**2**) a 9-mode model Hamiltonian that includes the extra mode ν_{20}; (**3**) a model Hamiltonian including only 2 modes (ν_{19} and ν_{21}). The modes ν_{19} and ν_{21} have B_3 symmetry and correspond to the 'flattening' motion of the ligands[?] and

View Article Online
DOI: 10.1039/C7CP00436B

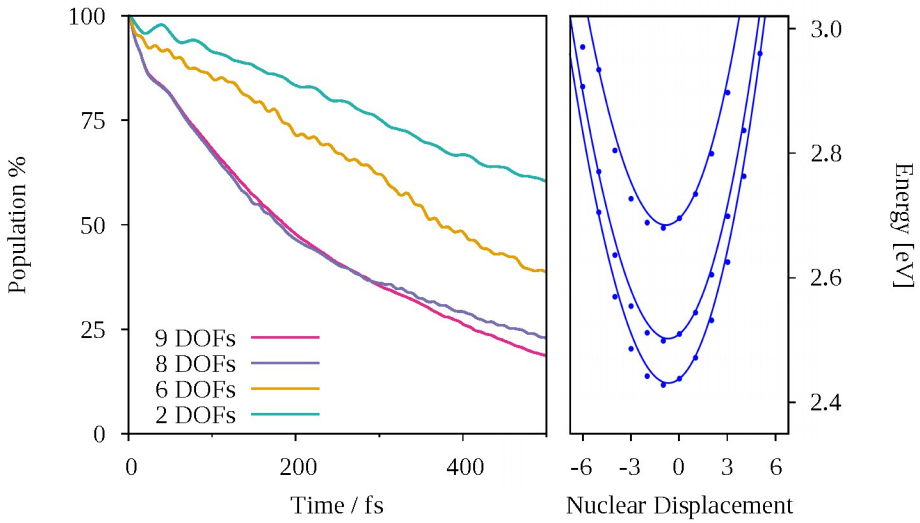

Fig. 6 (*Left*) Population decay of the photoexcited singlet state (S_3) using a model Hamiltonian with 8 degrees of freedom[28], 6 degrees of freedom (without modes ν_{19} and ν_{21}, and with two degrees of freedom (modes ν_{19} and ν_{21}). (*Right*) Cut through the PES along mode ν_{20}. The dots corresponds to quantum chemistry calculation, the lines to the fit from which the expansion coefficients are determined.

to an off center movement of the Cu atom, respectively; (**4**) 6-mode model Hamiltonian composed by all modes in (**1**) with the exception of modes ν_{19} and ν_{21}. The latter two models were devised following the observation that the weights of the vibrational modes ν_{19} and ν_{21} (Fig. 5) were amongst the largest for most of the trajectories. Figure 6 (Left) shows the population decay of the photoexcited singlet state S_3 obtained for the 4 model Hamiltonians ((**1**) to (**4**)). Notably, the population decay simulated with Hamiltonians (**1**) and (**2**) is very similar. However, slight differences can be observed after ~250 fs of dynamics, when we observe a slowing down of the population decay in the dynamics performed with the 9-mode Hamiltonian (**2**). In fact, mode ν_{20} is thought to play little role during the first instants following photoexcitation. Instead, it contributes substantially to the vibronic cooling of the system through the coupling with the bath (solvent) modes[56], a process that occurs in the picoseconds time scale. (Note that PCA can also identify diffusive modes, as well as other modes with a period longer than the analyzed time window, as long as they contribute to the covariant matrix). We can also draw a general conclusion about the inclusion of additional 'low-weight' modes (Fig. 6) in the MCTDH dynamics. When these modes couple to the other vibrational modes used to build the 'minimal' quantum Hamiltonian (model (**1**)), they further contribute to the spreading of the nuclear wavepacket, which tend to over-diffuse and dephase. This is an effect similar to the one observed in TSH dynamics performed in the full configuration space, where (due to the diffusion) a very large number of trajectories is required in order to converge properties and rates at long time scales.

From the analysis of the PCs of the TSH trajectories, we noticed that the weights of the vibrational modes ν_{19} and ν_{21} (Fig. 5, left panel) are among the largest for most of the trajectories (these modes are present in all Hamiltonians studies so far). To test the possibility to further reduce the number of relevant modes to include in the MCTDH dynamics, we analized the reduced model Hamiltonians (**3**) and (**4**). Looking at the corresponding population decays (Fig. 6, left panel), we observe that while these two modes (ν_{19} and ν_{21}) alone are not able to capture the correct decay, their inclusion in the Hamiltonian is essential. In fact, the 6-mode Hamiltonian (**4**) gives overall an unsatisfactory, unconverged, picture of the relaxation process. We conclude therefore that, in order to be effective these two modes need to be coupled to the remaining modes, which – despite their small amplitudes – are essential to describe correctly the nonadiabatic dynamics of the system.

4 Discussion and Conclusions

In the previous sections we have outlined the main results of our QM/MM excited state AIMD of $[Cu(dmp)_2]^+$. Here we combine the information obtained from the two different, but also complementary, approaches (MCTDH and TSH) and discuss about their potential advantages, disadvantages and synergies. However, when comparing these two sets of simulations is important to keep in mind that the calculation of corresponding PESs is performed at different levels of theory. In fact, the PES used for the MCTDH simulations[27,28] are interpolated along a reduced number of collective vibrational modes. In contrast, the TSH simulations require *on-the-fly* computations of the energies, forces, and nonadiabatic couplings at each time step. This implies a very different computational load for the two approaches. Consequently, the MCTDH simulations can afford calculations of the excited state electronic properties using hybrid functionals (in our case B3LYP), while the TSH simulations (performed with the plane-wave code CPMD) are restricted to a semi-local functionals from the GGA family (PBE in this case).

Despite these differences, it is important to note that for this specific system, the performances of PBE (as well as BLYP) and the hybrid B3LYP functionals are very similar, allowing us to com-

View Article Online
DOI: 10.1039/C7CP00436B

pare directly the results obtained using these two different approximations for the *x-c* functionals. Indeed, the only major difference between PBE and B3LYP for MLCT states is that in the former, the excited states energies are underestimated, due to the limitations of LR-TDDFT for charge transfer excited states (while keeping the energy separations between the excited PESs essentially unaltered). This would make dynamics between the excited and ground state unreliable, but in the present case we are only interested in the dynamics within the excited states, i.e. prior to the relaxation into the ground state.

Our present TSH simulations show that within the first 100 fs of dynamics, the initially excited electronic state, decays rapidly into the lowest ^{1}MLCT state. This state (S_1) is characterised by the excitation of one electron from a metal d-orbital to a π_g^* orbital of a single ligand. The ultrafast internal conversion dynamics observed with TSH (with a decay time of about $\sim$100 fs) is in excellent agreement with both experiment[21–26] and recent quantum dynamics simulations[27–30]. This process is driven by the significantly large nonadiabatic couplings between the low lying MLCT states, the small nuclear motion required to reach the crossing point between the force state and other states, and, finally, the high density of states at the Franck-Condon geometry.

Unfortunately, the direct evaluation of the ISC rate is not directly accessible from our TSH calculations, since we only performed a single trajectory using the TSH/ISC method, which includes the calculation of SOC and ISC transition probabilities *on-the-fly*. However, by post-processing the trajectories calculated using the 'standard' TSH scheme, we were able to identify some interesting aspects. In agreement with the recent quantum dynamics simulations[27], the TSH simulations show multiple crossings between the singlet state and the manifold of triplet states. The cumulative probability for ISC evaluated using the LZ formula amounts to more than 90% for three of the nine analysed trajectories with an average cumulative probability of 53% for the entire ensemble. This means that about half of the trajectories would undergo at least one ISC event during the first 100 fs of dynamics. However, we also note large differences among the different trajectories: three have a cumulative probability smaller than 30%, and one less than 5%. It is also stressed that the cumulative probability should be considered as an overestimation of the total effective ISC probability, since in this calculation we do not consider events of higher order, which would involve back transitions from triplet to singlet states. The occurrence of this type of events is clearly shown in the trajectory obtained using the TSH/ISC method (Fig. 3). In this case, we observe that after a first ISC to T_8, the system relaxes into T_7 before undergoing another ISC back to a singlet state (S_3). This single trajectory exemplifies well the complexity of the photophysics of this class of metal-complexes, which shows a convoluted sequence of IC and ISC events during the first 100 fs of dynamics after photoexcitation. This observation is consistent with our previous quantum dynamics simulations, which show that only $\sim$10% of the wavepacket had crossed into the triplet states within the first 100 fs.

Before moving further into the comparison of the results obtained with the two different, but also complementary, excited states dynamics approaches (TSH and wavepacket propagation), it is worth summarizing some of the main differences that characterize them: i) the dimensions of the sampled configuration space, which is confined to less than 10 dimensions in the quantum dynamics; ii) the nature of the dynamics, which in TSH is approximated with an ensemble of classical trajectories that can undergo nonadiabatic transitions (ICs and ISCs) among the different electronic states, and iii) the inclusion solvent effects that in TSH dynamics are treated within the QM/MM framework (explicit solvation), while in wavepacket dynamics is often approximated with a bath of harmonic oscillators.

Despite these differences, we find that the IC rate obtained with TSH are in good agreement with those described using the quantum dynamics approach. The ISC rate is also consistent, but the limited timescale of the simulations make it difficult to drawn strong conclusions on this aspect. This agreement points to a robustness of the dynamics, which in the case of the observables of interest for this study does not seem to depend crucially on the nature of the propagation schemes. More specifically, classical trajectories provide a good description of the dynamics far from the regions of strong coupling, while the surface hopping algorithm is able to capture most of the quantum effects at the avoided crossings. In particular, the missing quantum coherence of the TSH trajectories (due to the independent trajectory approximation) does not seem to affect the spreading of the trajectory ensemble significantly, at least in the sub-picosecond timescale. On the other hand, the confinement of the MCTDH dynamics into a subspace of the full molecular configuration space is not introducing important biases, when the correct set of collective vibrational modes is selected, as we showed using PCA.

Summarizing, both TSH and MCTDH approaches agree with the following picture of the photodynamics of $[Cu(dmp)_2]^+$: upon photoexcitation into the optically bright singlet states, which is made of a combination of electron excitations from d to π^*-gerade orbitals, the system quickly loses potential energy and relaxes into a singlet state characterized by the localization of the MLCT electron on a single ligand (see Appendix). The selection of the ligand depends mainly on the reorganization of the solvent molecules in the first solvation shell of the metal ion. This process occurs in less than 100 fs. ISC events can take place all along the relaxation path before the system reaches the lowest singlet state manifold. SOCs and thus ISC probabilities depend strongly on the character of the electronic state configurations, and favours transitions between high energy lying singlet and triplet states (in both directions). In fact, only a few transitions between S_1 and T_1 are observed. As a consequence, ISCs mainly occur in a sub-picosecond scale before the full relaxation of the system into S_1 is accomplished. However, we do not exclude that on a longer time-scale (not covered by the present simulations) residual transitions between S_1 and the high energy triplet states are still possible, even though with very low probabilities due to the relatively small size of the SOCs.

The extremely low luminescence quantum yield, 10^{-4}, of $[Cu(dmp)_2]^+$ in acentonitrile is also, in part a consequence of the solvent effects. By taking advantage of the QM/MM scheme, we could observe an ultrafast solvent reorganization process tak-

View Article Online
DOI: 10.1039/C7CP00436B

ing place in the first solvation shell of the metal center that leads to the formation of attractive interactions with the positively charged Cu ion. This process has the effect of further stabilizating the lowest excited states of the complex, increasing therefore the probability for a non-radiative decay. It is worth stressing that this type of analysis is only possible in the framework of TSH dynamics, which can be coupled to an explicit representation (classical or QM) of the solvent. The combination of MCTDH with an explicit solvent model is highly desirable, however, its implementation is hampered by the difficulty to parametrise a coupling Hamiltonian able to describe the loosely bound and often anharmonic solvent modes.

As already mentioned, our previous quantum dynamics simulations have been able to produce an accurate description of the excited state dynamics[27,28]. However, such simulations rely on an appropriate selection of the relevant active vibrational modes to include in the vibronic coupling Hamiltonian. Unfortunately, with a couple of exceptions[11,12], there has been no systematic approach to guide in the selection of these collective modes. Indeed, their choice is usually made by inspection of the ground state normal modes and it is guided by qualitative arguments based on their frequencies and symmetries. In this work, we addressed the issue of selecting the relevant normal mode to be used in the quantum dynamics by means of a PCA carried out on the excited states TSH trajectories. By projecting the first most representative PCs onto the ground state normal modes, we were able to identify most of the collective vibrations previously selected for the MCTDH simulations of $[Cu(dmp)_2]^+$ complex[27,28]. However, it is important to mention that we could not find (so far) any clear and direct correlation between the weights of the different PC modes (which are measured in terms of the size of the corresponding eigenvalues) and their relevance for the quantum dynamics; it is well possible that PC modes exist that only participate marginally to the overall TSH dynamics, while being essential for the quantum dynamics, especially for the description of the small amplitude ultrafast components. On the contrary, by applying PCA to the TSH trajectories and projecting the corresponding eigenvectors into the normal modes of the system, we were able to identify an additional mode, ν_{20}, that contributes in an important manner to the description of the TSH dynamics and that was not considered in the previous MCTDH calculations reported in ref.[27,28]. However, our analysis confirmed that this mode was not essential for the description of the first 100 fs of quantum dynamics. In fact, it can be considered as a 'bath mode' that is activated by the interaction with the solvent (which is explicit in TSH dynamics), but which does not influence the quantum dynamics at least in the sub-ps time scale. In conclusion, we showed that PCA can become a powerful tool for the identification of the vibrational modes to include in the relevant subspace used to perform wavepacket quantum dynamics. This approach can help to rationalize the photophysics of the system of interest, providing a description of the dynamics in the minimal configuration sub-space possible. In addition, this fully automatized 'dimensional reduction' procedure will help improving the efficiency of future MCTDH calculations.

5 Acknowledgements

The authors thank the Swiss National Science Foundation for funding through Grants 200021-137717 and No. 200021-146396, and the Swiss National Centres of Competence in Research (NCCR) for funding through the projects MUST and MARVEL.

6 Appendix

Electronic Structure Properties of $[Cu(dmp)_2]^+$: diabatic versus adiabatic representations

For a detailed understanding of the present excited state TSH simulations we need to analyze the electronic character of the different states involved in this dynamics. The comparison with the recently published quantum dynamics simulations[27] is made difficult due to the different electronic representations used in the two approaches: adiabatic in TSH and diabatic in MCTDH. In particular, when the adiabatic representation is adopted (TSH) the electronic character of a given state (numbered according to its energy) can change during the dynamics. On the other hand, quantum dynamics simulations (wavepacket propagations) are preferentially performed in the diabatic representation and, as a consequence, the character of the states is well defined along the entire dynamics.

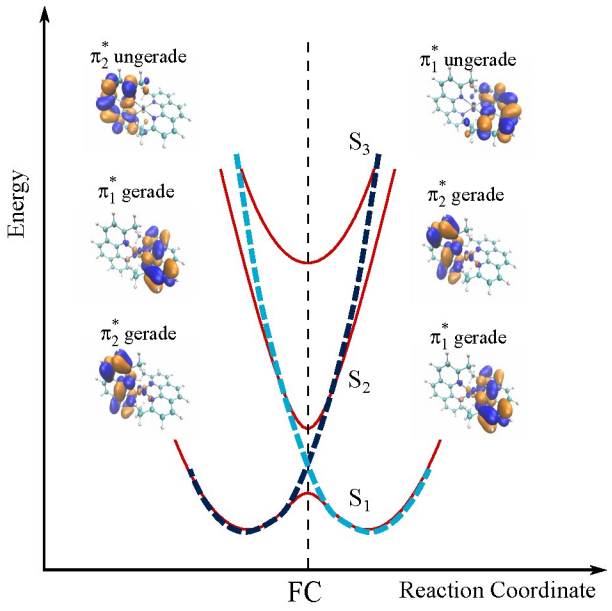

Fig. 7 Adiabatic singlet potential energy surfaces (solid red lines) calculated along the normal mode ν_{21} [28,30]. Near the Franck-Condon point, all excited states have a strong mixed character that evolves, when progressing along the coordinate, into the 'purified' ligand-centered π^* antibonding orbitals shown in the insets. A graphical representation of the corresponding diabatic potential energy surfaces is also added (dashed lines).

This situation is illustrated in Fig. 7, which shows a schematic representation of the singlet adiabatic and diabatic states along one of the main collective modes used in the MCTDH dynamics[27], namely the flattening of the dihedral angle between the two ligands (pseudo Jahn-Teller distortion, ν_{21}). To simplify the

View Article Online
DOI: 10.1039/C7CP00436B

notation, we will label the states involved in this analysis as S_1, S_2 and S_2. In reality, there will be other (spectator) states intercalated between the selected ones, which however are omitted from this analysis. The photoexcited S_3 state, from which the dynamics is started, has a mixed character derived from the promotion of an electron from the degenerate (at D_{2d} symmetry) HOMO (d_{xz}) and HOMO-1 (d_{yz}) orbitals centred at the copper atom, into a pair of degenerate anti-bonding π orbitals of *gerade* symmetry (π_g^*) on the ligands. In the D_{2d} symmetry, the π_g^* orbitals are delocalised on both ligands and their contribution to the S_3 state, at the Franck-Condon geometry, is very similar. As for S_3, the lowest singlet states, S_1 and S_2, are also made of mixed state configurations arising from the photoexcitation of d_{xz} and d_{yz} electrons into the π^*-*gerade* orbitals.

As shown in Fig. 7 the character of these states depend upon structural changes. In particular, in the excited states we observed a lifting of orbital degeneracy associated to the pseudo Jahn-Teller (JT) distortion that determines the symmetry reduction from D_{2d} to D_2. Additional symmetry breaking mechanisms can also occur in solution through the coupling to different instantaneous solvent configurations, which favour the localization of the photoexcited electron on a single ligand[15,57]. A detailed account on the solvent effects of the photophysics on copper phenenthrolines is given in section 3.2.

To further clarify this observation, we perform a characterization of the first three singlet excited states along the pseudo-JT distortion coordinate ν_{21} shown in Fig. 7. Moving to the left and to the right of the FC point we observe a different localization of the photoexcited π^* electron on the two ligands. As reported in Table 3, the adiabatic states are characterized by excitations from the HOMO (d_{xz}) orbital to the π^* antibonding orbitals on the ligands. While at FC the transitions are mixed, at the S_1 minima (left and right) they acquire a more defined character. For the minima at the RHS in Fig. 7, the S_1 state is characterized by a $d_{xz} \rightarrow \pi_{1g}^*$ transition, where π_{1g}^* denotes the π^*-*gerade* orbital centered at the ligands labelled with the index 1; S_2 is characterized by an equivalent $d_{xz} \rightarrow \pi_{2g}^*$ transition centered on the opposite ligand (labelled with 2); and S_3 acquires a $d_{xz} \rightarrow \pi_{1u}^*$ character. An equivalent behavior (but with a localization of the π^* orbital on the opposite ligand) is also observed at the second minima on S_1 (on the LHS of the PC point). This analysis is not restricted to the family of the singlet excited states; in fact, a similar decrease in mixing of the $d_{xz} \rightarrow \pi_{g/u}^*$ transitions is also observed at the geometries that correspond to the minima of the T_1 state (Table 3).

Coming to the dynamics, in the diabatic representation each electronic state preserves its character along the collective coordinate and different diabatic states cross at the FC configuration (dashed lines in Fig. 7). The mixed character of the adiabatic states at the FC is therefore reflected into a crossing of different states in the diabatic picture. In the same way, internal conversion processes, which in the adiabatic picture is described by the transfer of wavepacket population (or trajectories in the TSH framework) from S_3 to S_2 and S_1 triggered by the nonadiabatic couplings, translate in the diabatic picture into the relaxation of the nuclear wavepacket along a single diabatic PES with preservation of the orbital symmetry.

References

1 Kosloff, R. *J. Phys. Chem.* **1988**, *92*, 2087–2100.
2 Worth, G. A.; Cederbaum, L. S. *Annu. Rev. Phys. Chem.* **2004**, *55*, 127–158.
3 Raab, A.; Worth, G.; Meyer, H.-D.; Cederbaum, L. *J. Chem. Phys.* **1999**, *110*, 936.
4 Markmann, A.; Worth, G. A.; Cederbaum, L. S. *J. Chem. Phys.* **2005**, *122*, 144320–144320–15.
5 Worth, G. A.; Welch, G.; Paterson, M. J. *Mol. Phys.* **2006**, *104*, 1095–1105.
6 Penfold, T. J.; Spesyvtsev, R.; Kirkby, O. M.; Minns, R. S.; Parker, D. S. N.; Fielding, H. H.; Worth, G. A. *J. Chem. Phys.* **2012**, *137*, 204310–204310–12.
7 Papai, M.; Vanko, G.; Rozgonyi, T.; TJ, P. *J. Phys. Chem. Lett.* **2016**,
8 Gibson, J.; Monkman, A. P.; Penfold, T. J. *ChemPhysChem* **2016**, *17*, 2956–2961.
9 Tavernelli, I. *Phys. Rev. B* **2006**, *73*, 094204.
10 Beck, M. H.; Jaeckle, A.; Worth, G. A.; Meyer, H. D. *Phys. Rep.* **2000**, *324*, 1–105.
11 Harabuchi, Y.; Eng, J.; Gindensperger, E.; Taketsugu, T.; Maeda, S.; Daniel, C. *Journal of chemical theory and computation* **2016**, *12*, 2335–2345.
12 Fumanal, M.; Gindensperger, E.; Daniel, C. *Journal of chemical theory and computation* **2017**,
13 Makri, N.; Miller, W. H. *J. Chem. Phys.* **1987**, *87*, 5781–5787.
14 Kapral, R. *Ann. Rev. of Phys. Chem.* **2006**, *57*, 129–157.
15 Tavernelli, I.; Curchod, B. F. E.; Rothlisberger, U. *Chemical Physics* **2011**, *391*, 101–109.
16 Car, R.; Parrinello, M. *Phys. Rev. Lett.* **1985**, *55*, 2471–2474.
17 Drukker, K. *J. Comput. Phys.* **1999**, *153*, 225–272.
18 Tully, J. C.; Preston, R. K. *J. Chem. Phys.* **1971**, *55*, 562–572.
19 Tully, J. C. *J. Chem. Phys.* **1990**, *93*, 1061–1071.
20 Tavernelli, I. *Acc. Chem. Res.* **2015**, *48*, 792–800.
21 Chen, L. X.; Jennings, G.; Liu, T.; Gosztola, D. J.; Hessler, J. P.; Scaltrito, D. V.; Meyer, G. J. *J. Am. Chem. Soc.* **2002**, *124*, 10861–10867.
22 Siddique, Z. A.; Yamamoto, Y.; Ohno, T.; Nozaki, K. *Inorg. Chem.* **2003**, *42*, 6366–6378.
23 Hua, L.; Iwamura, M.; Takeuchi, S.; Tahara, T. *Phys. Chem. Chem. Phys.* **2015**, –.
24 Iwamura, M.; Takeuchi, S.; Tahara, T. *J. Am. Chem. Soc.* **2007**, *129*, 5248–5256.
25 Iwamura, M.; Takeuchi, S.; Tahara, T, *Phys. Chem. Chem. Phys.* **2014**, *16*, 4143–4154.
26 Iwamura, M.; Watanabe, H.; Ishii, K.; Takeuchi, S.; Tahara, T. *J. Am. Chem. Soc.* **2011**, *133*, 7728–7736.
27 Capano, G.; Chergui, M.; Rothlisberger, U.; Tavernelli, I.; Penfold, T. J. *J. Phys. Chem. A* **2014**, *118*, 9861–9869.
28 Capano, G.; Penfold, T. J.; Rothlisberger, U.; Tavernelli, I. *CHIMIA International Journal for Chemistry* **2014**, *68*, 227–230.
29 Capano, G.; Milne, C.; Chergui, M.; Rothlisberger, U.; Taver-

View Article Online
DOI: 10.1039/C7CP00436B

Table 3 Energies and characters of the first three (bright) excited singlet states at: (*i*) the optimized Franck-Condon (FC) geometry (Data from ref.[28]), (*ii*) the S_1 minimum along the ν_{21} mode, and (*iii*) the triplet (T_1) excited state minimum along the same mode.

	FC geometry		S_1 minimum		T_1 minimum	
	Energy (eV)	Character	Energy (eV)	Character	Energy (eV)	Character
S_1	2.44	$d_{xz} \rightarrow \pi^*_{g+}, d_{yz} \rightarrow \pi^*_{g-}$	2.24	$d_{xz} \rightarrow \pi^*_{1g}$	1.88	$d_{xz} \rightarrow \pi^*_{g+}$
S_2	2.51	$d_{yz} \rightarrow \pi^*_{g+}, d_{xz} \rightarrow \pi^*_{g-}$	2.63	$d_{xz} \rightarrow \pi^*_{2g}$	1.91	$d_{xz} \rightarrow \pi^*_{g-}$
S_3	2.70	$d_{xz} \rightarrow \pi^*_{g+}, d_{yz} \rightarrow \pi^*_{g-}$	2.71	$d_{xz} \rightarrow \pi^*_{1u}$	2.25	$d_{xz} \rightarrow \pi^*_{u+}$

nelli, I.; Penfold, T. *J. Phys. B* **2015**, *48*, 214001.
30 Capano, G.; Rothlisberger, U.; Tavernelli, I.; Penfold, T. J. *J. Phys. Chem. A* **2015**, *119*, 7026–7037.
31 Du, L.; Lan, Z. *Phys. Chem. Chem. Phys.* **2016**,
32 Tapavicza, E.; Tavernelli, I.; Rothlisberger, U. *Phys. Rev. Lett.* **2007**, *98*, 023001.
33 Tavernelli, I.; Curchod, B. F. E.; Laktionov, A.; Rothlisberger, U. *J. Chem. Phys.* **2010**, *133*, 194104.
34 Curchod, B. F. E.; Rothlisberger, U.; Tavernelli, I. *ChemPhysChem* **2013**, *14*, 1314–1340.
35 http://www.cpmd.org/. Copyright IBM Corp 1990-2008, Copyright MPI f§r FestkŽrperforschung Stuttgart 1997-2001.
36 Perdew, J. P.; Burke, K.; Ernzerhof, M. *Phys. Rev. Lett.* **1996**, *77*, 3865–3868.
37 Troullier, N.; Martins, J. L. *Phys. Rev. B* **1991**, *43*, 1993–2006.
38 von Lilienfeld, O. A.; Tavernelli, I.; Rothlisberger, U.; Sebastiani, D. *Phys. Rev. Lett.* **2004**, *93*, 153004.
39 Lin, I.-C.; Coutinho-Neto, M. D.; Felsenheimer, C.; von Lilienfeld, O. A.; Tavernelli, I.; Rothlisberger, U. *Phys. Rev. B* **2007**, *75*, 205131.
40 Nose, S. *J. Chem. Phys.* **1984**, *81*, 512.
41 Hoover, W. *Phys. Rev. A* **1985**, *31*, 1695–1697.
42 Shaw, G. B.; Grant, C. D.; Shirota, H.; Castner, E. W.; Meyer, G. J.; Chen, L. X. *J. Am. Chem. Soc.* **2007**, *129*, 2147–2160.
43 Franco de Carvalho, F.; Tavernelli, I. *J. Chem. Phys.* **2015**, *143*, 224105.
44 Lin, H.; Truhlar, D. G. *Theor Chem Acc* **2006**, *117*, 185–199.
45 Case, D. A. et al. *AMBER 12 University of California, San Francisco.*; 2012.
46 Laio, A.; VandeVondele, J.; Rothlisberger, U. *J. Chem. Phys.* **2002**, *116*, 6941–6947.
47 Pearson, K. *Philosophical Magazine Series 6* **1901**, *2*, 559–572.
48 Hotelling, H. *J. Educ. Psychol.* **1933**, *24*, 417–441.
49 Hotelling, H. *Biometrika* **1936**, *28*, 321–377.
50 Richter, M.; Marquetand, P.; González-Vázquez, J.; Sola, I.; González, L. *J. Chem. Theory Comput.* **2011**, *7*, 1253–1258.
51 Granucci, G.; Persico, M.; Spighi, G. *J. Chem. Phys.* **2012**, *137*, 22A501.
52 Curchod, B. F.; Rauer, C.; Marquetand, P.; González, L.; Martínez, T. J. *J. Chem. Phys.* **2016**, *144*, 101102.
53 Cui, G.; Thiel, W. *J. Chem. Phys.* **2014**, *141*, 124101.
54 Carvalho, F. F. d.; Curchod, B. F. E.; Penfold, T. J.; Tavernelli, I. *J. Chem. Phys.* **2014**, *140*, 144103.
55 Englman, R.; Jortner, J. *Mol. Phys.* **1970**, *18*, 145–164.
56 Lasorne, B.; Sicilia, F.; Bearpark, M. J.; Robb, M. A.; Worth, G. A.; Blancafort, L. *J. Chem. Phys.* **2008**, *128*, 124307–124307–10.
57 Moret, M.-E.; Tavernelli, I.; Chergui, M.; Rothlisberger, U. *Chem. Eur. J.* **2010**, *16*, 5889–5894.

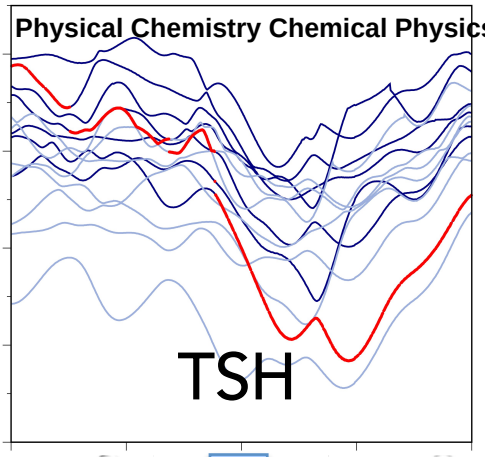

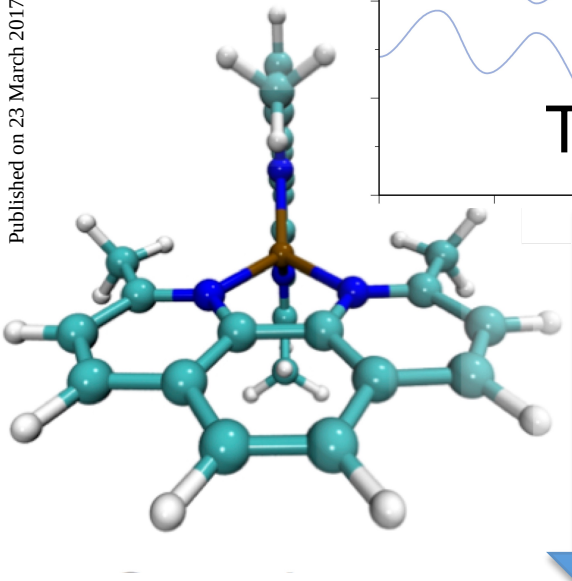

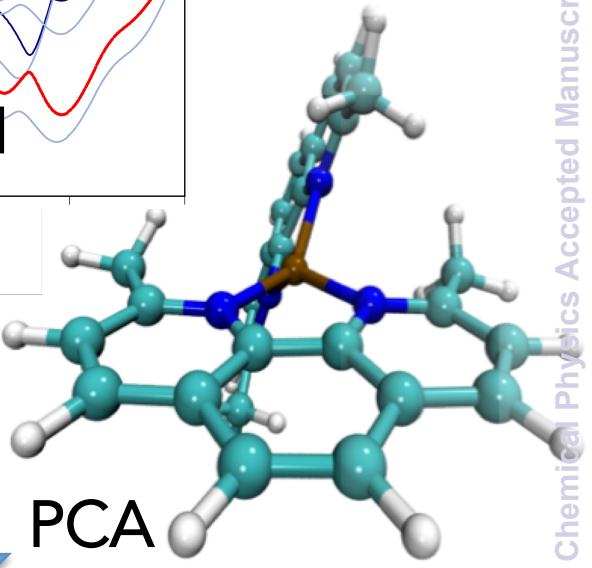

PCA